Liouvillian exceptional points in quantum brickwork circuits

Vladislav Popkov [1,2] and Mario Salerno [3]

[1]*Faculty of Mathematics and Physics, University of Ljubljana, Jadranska 19, SI-1000 Ljubljana, Slovenia*

[2]*Department of Physics, University of Wuppertal, Gaussstraße 20, D-42119 Wuppertal, Germany*

[3]*Dipartimento di Fisica "E. R. Caianiello," and INFN Sezione di Napoli - Gruppo Collegato di Salerno, University of Wuppertal, Università di Salerno, Via Giovanni Paolo II, I-84084 Fisciano (SA), Italy*

(Received 15 October 2025; accepted 14 April 2026; published 29 April 2026)

We demonstrate that Liouvillian exceptional points (LEPs), previously explored only in continuous Lindbladian dynamics, also emerge in discrete brickwork completely positive trace-preserving (CPTP) circuits. By analytically solving a minimal two-qubit brickwork model, we identify the conditions under which discrete-time LEPs arise and show that they retain the hallmark square-root eigenvalue splitting and linear-in-time sensitivity enhancement. These results establish a direct bridge between continuous non-Hermitian physics and discrete quantum-circuit architectures, opening a path toward the realization of exceptional-point-based sensing on near-term quantum processors.

DOI: 10.1103/ksj2-w5cj

I. INTRODUCTION

In the presence of dissipation, the unitary evolution of a quantum system is broken, the map becomes effectively contracting, and the system is driven toward a steady state. Among the possible manifestations of such nonunitary evolution are *exceptional points* (EPs), i.e., parameter values where the Liouvillian superoperator becomes nondiagonalizable [1,2]. Liouvillian exceptional points (LEPs) in continuous Lindbladian dynamics promise enhanced sensitivity due to their nonanalytic dependence on perturbations, such as eigenvalue splitting $\propto\sqrt{\varepsilon}$ for a second-order LEP [3–5], analogous to the sensitivity enhancement observed in non-Hermitian photonics [6,7]. LEPs have recently been demonstrated in continuous-time experiments [8] and analyzed in few-qubit theoretical models [9]. EP-like degeneracies can also appear in auxiliary nonunitary transfer matrices used to compute correlation functions in closed, dual-unitary circuits [10]. In that last case, however, the EPs pertain to the mathematical construction rather than the physical evolution of the system.

Here, we focus on the discrete-time setting most relevant for current quantum devices, where evolution proceeds stroboscopically through brickwork completely positive trace-preserving (CPTP) maps [11–13]. While EPs in non-Hermitian maps and LEPs in continuous Lindbladians have been studied independently, the emergence of LEPs in brickwork CPTP circuits, and the fate of their associated sensing advantages, remain unexplored. The discrete time-step and CPTP constraints could, in principle, alter the Jordan structure or suppress per-step signal amplitudes, challenging the persistence of LEP physics in circuit-based architectures.

In this paper, we present an analytic demonstration that two-qubit brickwork CPTP circuits can host Liouvillian exceptional points that retain their characteristic sensing behavior. By constructing minimal steps (see Fig. 1) reproducing a target Lindbladian to first order in Δt, we analytically determine the manifold of LEPs and quantify the eigenvalue-splitting scaling in the discrete-time regime. Our results show that LEPs are a generic feature of stroboscopic CPTP dynamics, thereby bridging the gap between continuous Lindbladian evolution and the discrete operations implemented in all programmable quantum devices.

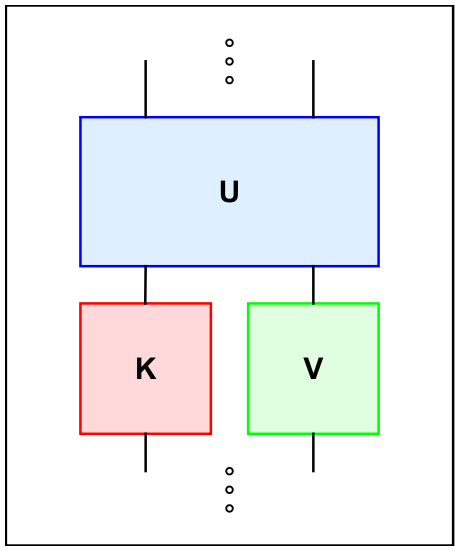


FIG. 1. Schematic of the two-step brickwork protocol. Even steps implement a two-qubit unitary gate U (XXZ type), while odd steps consist of a Kraus relaxation map on qubit 1 and a local unitary channel V on qubit 2. Periodic repetition of this protocol defines the brickwork CPTP map.

Published by the American Physical Society under the terms of the Creative Commons Attribution 4.0 International license. Further distribution of this work must maintain attribution to the author(s) and the published article's title, journal citation, and DOI.

II. MODEL EQUATIONS

We consider a two-qubit brickwork circuit (Fig. 1), composed of alternating unitary and dissipative layers. Even steps apply a two-qubit gate

$$U = \begin{pmatrix} 1 & 0 & 0 & 0 \\ 0 & a & b & 0 \\ 0 & b & a & 0 \\ 0 & 0 & 0 & 1 \end{pmatrix}, \tag{1}$$

parametrized by anisotropy q and spectral parameter λ as

$$a \equiv \frac{q - q^{-1}}{q\lambda - (q\lambda)^{-1}}, \quad b \equiv \frac{\lambda - \lambda^{-1}}{q\lambda - (q\lambda)^{-1}}.$$

The gate acts on a pair of neighboring qubits via a folded map as $\rho \to U\rho U^\dagger$. In the limit $\lambda \to 1 + \delta$ with $\delta \ll 1$ it describes the coherent time evolution of the density matrix ρ via Trotter decomposition of e^{-iHt} with H the two-qubit XXZ Hamiltonian. Indeed, let us parametrize $q = e^{i\gamma}$, $\lambda = e^{\delta}$, with $\delta \ll 1$. Expanding parameters a and b of U to first order in δ we get $a \approx 1 + i\delta a_0 + O(\delta^2)$, $b = -i\delta b_0 + O(\delta^2)$, with $a_0 = \cot(\gamma)$, $b_0 = 1/\sin(\gamma)$, and U becomes

$$U = \mathbb{1} - i\delta \begin{pmatrix} 0 & 0 & 0 & 0 \\ 0 & -a_0 & b_0 & 0 \\ 0 & b_0 & -a_0 & 0 \\ 0 & 0 & 0 & 0 \end{pmatrix} + O(\delta^2) \approx \mathbb{I} - i\,\delta\, h_{12}, \tag{2}$$

where h_{12} is a Hamiltonian density of the XXZ model,

$$h_{12} = J\left[\sigma_1^x\sigma_2^x + \sigma_1^y\sigma_2^y + \Delta\left(\sigma_1^z\sigma_2^z - \mathbb{I}\right)\right] \equiv h_{\mathrm{XXZ}}, \tag{3}$$

with $J = 1/(2\sin\gamma)$, $\Delta = \cos\gamma$. After n iteration steps, with $n\delta \equiv t$ fixed as $\delta \to 0$, we have $U^n \to e^{-ith_{\mathrm{XXZ}}}$, so that the density matrix undergoes a coherent unitary evolution, $\rho(t) = e^{-ih_{\mathrm{XXZ}}t}\rho(0)e^{ih_{\mathrm{XXZ}}t}$, under the XXZ Hamiltonian.

Odd steps act locally: qubit 1 undergoes a dissipative Kraus map

$$\mathcal{K}[\rho] = \sum_{j=1}^{2} K_j \rho K_j^\dagger, \quad K_1 = \sqrt{1-\epsilon^2}\,\sigma^+, \quad K_2 = \begin{pmatrix} 1 & 0 \\ 0 & \epsilon \end{pmatrix}, \tag{4}$$

while qubit 2 evolves under an arbitrary local unitary channel $\mathcal{V}[\rho] = V\rho V^\dagger$. The map (4) describes a relaxation of a qubit towards the targeted state $|\uparrow\rangle\langle\uparrow|$ after a typical number of steps $n_{\mathrm{relax}} = [-2/\log(\epsilon)]$, where $0 < \epsilon \leqslant 1$ parametrizes the strength of the relaxation (see Appendix A).

For $0 \leqslant \epsilon < 1$ the Kraus map is strictly dissipative (nonunitary), while in the limit $\epsilon = 0$ it reduces to a pure reset channel, realizable in current qubit-based quantum circuit experiments [14,15]. In this limit, any input qubit state ρ is deterministically mapped to the fully polarized state $\mathcal{K}[\rho] = |\uparrow\rangle\langle\uparrow|$, representing the most extreme form of nonunitary evolution (total dissipation). In the opposite limit $\epsilon = 1$, the Kraus map becomes unitary and coincides with the identity channel. A full brickwork step is

$$\rho_{t+1} = \mathcal{U}\rho_t = U\left(\sum_{j=1}^{2}(K_j \otimes V)\rho_t(K_j^\dagger \otimes V^\dagger)\right)U^\dagger, \tag{5}$$

or, in vectorized form, $|\rho[t+1]\rangle = \mathcal{T}|\rho[t]\rangle$, with discrete time Liouvillian (or superoperator)

$$\mathcal{T} = (U \otimes U^*)\left(\sum_{j=1}^{2}(K_j \otimes V) \otimes (K_j^* \otimes V^*)\right). \tag{6}$$

In the $\Delta t \to 0$ limit, this reduces to a continuous time Lindbladian with jump operator $L = \sigma^+$ acting on the first qubit and XXZ Hamiltonian interactions (see Appendix A).

III. SYMMETRY AND BLOCK DIAGONALIZATION OF THE LIOUVILLIAN

Both the Kraus gates and the two-qubit unitary U preserve a $\mathbb{Z}_2$ parity symmetry, $[\mathcal{K}, \Sigma_z] = [U, \Sigma_z] = 0$, with $\Sigma_z = \sigma_z \otimes \sigma_z$. For the full superoperator to inherit this symmetry we further require $[V, \sigma_z] = 0$, in which case V reduces to a pure Z rotation. The superoperator $\mathcal{T}$ can then be block diagonalized by introducing the parity projectors

$$P_\pm = \tfrac{1}{2}(I_{16} \pm \Sigma_z \otimes \Sigma_z), \tag{7}$$

which satisfy $P_+ + P_- = I_{16}$, $P_\pm P_\mp = 0$, and $[P_\pm, \mathcal{T}] = 0$. Consequently,

$$\mathcal{T} = P_+\mathcal{T}P_+ + P_-\mathcal{T}P_- \equiv \mathcal{T}_+ + \mathcal{T}_-, \tag{8}$$

where $\mathcal{T}_\pm$ are rank-8 matrices acting on the even and odd parity subspaces, respectively. After removing null rows and columns, the superoperator takes the block-diagonal form

$$\mathcal{T} = \begin{pmatrix} \tau_+ & 0 \\ 0 & \tau_- \end{pmatrix}, \tag{9}$$

where $\tau_\pm$ are 8×8 matrices of the form

$$\tau_\pm = \begin{pmatrix} A_\pm & B_\pm \\ C_\pm & D_\pm \end{pmatrix}, \tag{10}$$

with $A_\pm, B_\pm, C_\pm, D_\pm$, and 4×4 matrices given explicitly in Appendix B, most of which are sparse. For example, A_+ is diagonal, B_+ has a single nonzero element, and C_+ has only one nonzero row, while D_+ is a full matrix. Because of the sparsity of the off-diagonal blocks, the eigenvalues of $\tau_\pm$ can be efficiently computed using the Schur complement discussed in the next section. Further simplifications lead to remarkably simple expressions for the superoperator spectrum (see below).

IV. SUPEROPERATOR SPECTRUM AND THE EP MANIFOLD

Although for $\mathbb{Z}_2$ symmetry the gate V can in general be written as $V = e^{i\theta\sigma_z}$, to gain analytical insight into the spectrum and the location of exceptional points (EPs) we focus, in the following, on the case $V = I$ (i.e., $\theta = 0$), which we refer to as the *superintegrable* case. This choice preserves the full dependence on (ϵ, q, λ) while considerably simplifying the secular equations of $\tau_\pm$, since in this limit the characteristic polynomials factorize into quadratic polynomials. Within this setting, the entire spectrum can be obtained analytically, enabling a complete identification and classification of the non-Hermitian degeneracies that define the EP manifold of the brickwork superoperator.

In particular in the easy-plane regime ($|q| = 1$, $\lambda \in \mathbb{R}$, $0 < \epsilon \leqslant 1$), the superoperator spectrum acquires a following simple structure: all eigenvalues are either analytic or involve a single square root. Explicitly, the eigenvalues of $\tau_\pm$ blocks can be analytically computed using the Schur-complement formula

$$\det(\mu I_8 - \tau_\pm) = \det(\mu I_4 - A_\pm)\det[\mu I_4 - D_\pm - C_\pm(\mu I_4 - A_\pm)^{-1}B_\pm] = 0. \tag{11}$$

For the eigenvalues of τ_+, the first factor of Eq. (11) directly yields

$$\mu_{1,2,3,4} = \{1, \epsilon^2, \epsilon, \epsilon\}. \tag{12}$$

The remaining four eigenvalues follow from the second determinant on the right-hand side of (11) which factorizes as

$$P(\mu) = (\mu - \epsilon)^2\,(\mu^2 + \xi\,\mu + \epsilon^2), \tag{13}$$

with ξ given by

$$\xi = \frac{\lambda^2 q^4(\epsilon^2+1) + 2q^2[\lambda^4\epsilon - \lambda^2(\epsilon+1)^2 + \epsilon] + \lambda^2(\epsilon^2+1)}{(\lambda^2 - q^2)(\lambda^2 q^2 - 1)}. \tag{14}$$

Introducing the functions f, Q as given in Eqs. (21) and (22) we have that the remaining eigenvalues can be written in the form

$$\mu_{5,6} = \epsilon,\ \ \mu_{7,8} = \frac{(Q \mp f\lambda)^2}{4(q^2 - \lambda^2)(\lambda^2 q^2 - 1)}.$$

Similarly, the characteristic polynomial of τ_-, after clearing common denominators, factorizes into four quadratic monic polynomials,

$$P_1(\mu) = \mu^2 + \frac{f\lambda}{\lambda^2 - q^2}\mu + \epsilon\frac{\lambda^2 q^2 - 1}{q^2 - \lambda^2}, \tag{15}$$

$$P_2(\mu) = \mu^2 + \epsilon\frac{f\lambda}{\lambda^2 - q^2}\mu + \epsilon^3\frac{\lambda^2 q^2 - 1}{q^2 - \lambda^2}, \tag{16}$$

$$P_3(\mu) = \mu^2 + \frac{f\lambda}{1 - \lambda^2 q^2}\mu + \epsilon\frac{q^2 - \lambda^2}{1 - \lambda^2 q^2}, \tag{17}$$

$$P_4(\mu) = \mu^2 + \epsilon\frac{f\lambda}{1 - \lambda^2 q^2}\mu + \epsilon^3\frac{q^2 - \lambda^2}{1 - \lambda^2 q^2}, \tag{18}$$

with f given in Eq. (22). It is worth noting that the linear and constant coefficients of the polynomial P_2 are obtained from those of P_1 by multiplication with ϵ and ϵ^2, respectively, and an analogous relation holds between the pairs P_3, P_4. This rescaling of monic quadratic polynomials implies that the roots of P_2 and P_4 coincide with those of P_1 and P_3, respectively, up to a factor ϵ. Denoting $\mu_{9,\ldots,16}$ as the eigenvalues of τ_-, this implies $\mu_{11,12} = \epsilon\,\mu_{9,10}$, $\mu_{15,16} = \epsilon\,\mu_{13,14}$, with the other eigenvalues following from P_1 and P_3 roots as

$$\mu_{9,10} = \frac{f\lambda \pm Q}{2(\lambda^2 q^2 - 1)}, \quad \mu_{13,14} = \frac{f\lambda \pm Q}{2(q^2 - \lambda^2)}. \tag{19}$$

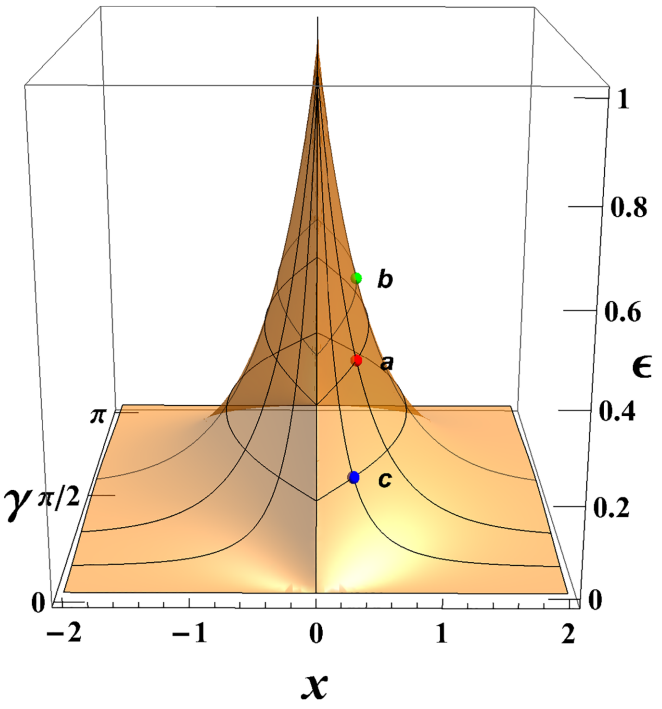


FIG. 2. Superoperator exceptional points manifold in parameter space $\{x \equiv \log\lambda, \gamma, \epsilon\}$ with $\epsilon \in [0, 1]$ and $q = e^{i\gamma}$. Coordinates of representative points on the LEP manifold are $a = \{0.3293, \pi/4, 0.4\}$, $b = \{0.3466, \pi/2, 0.5\}$, and $c = \{0.3013, \pi/9, 0.2\}$. Bifurcation diagrams of $\mathcal{T}$ eigenvalues for EP a are shown in Fig. 3, while for those of EPs b and c are depicted in Fig. 6.

In summary, the analytical expressions of the superoperator eigenvalues are

$$\mu_1 = 1, \quad \mu_2 = \epsilon^2, \quad \mu_3 = \mu_4 = \mu_5 = \mu_6 = \epsilon,$$
$$\mu_{7,8} = \frac{(Q \mp f\lambda)^2}{4(q^2 - \lambda^2)(\lambda^2 q^2 - 1)}, \quad \mu_{9,10} = \frac{f\lambda \mp Q}{2(\lambda^2 q^2 - 1)}, \tag{20}$$
$$\mu_{11,12} = \epsilon\mu_{9,10}, \quad \mu_{13,14} = \tfrac{f\lambda \mp Q}{2(q^2 - \lambda^2)}, \quad \mu_{15,16} = \epsilon\mu_{13,14},$$

with

$$Q = \sqrt{\lambda^2(\epsilon-1)^2(q^4+1) + 2q^2(2\lambda^4\epsilon - \lambda^2(\epsilon+1)^2 + 2\epsilon)}, \tag{21}$$

$$f = (q^2 - 1)(\epsilon + 1). \tag{22}$$

Denoting $q = e^{i\gamma}$, $\lambda = e^x$, one finds $Q = \sqrt{2}\lambda q\sqrt{F}$ with

$$F = 2[(\epsilon-1)^2\cos(2\gamma) + 4\epsilon\cosh(2x) - (\epsilon+1)^2]. \tag{23}$$

The zeros of F correspond to second-order LEPs, i.e., coalescence of two eigenvalues into a Jordan block of size 2×2. Solving $F = 0$ yields the EP manifold

$$\epsilon_{\mathrm{EP}} = \frac{\cosh(2x) - \cos^2\gamma - \sqrt{2}|\sinh x|\sqrt{\cosh(2x) - \cos(2\gamma)}}{\sin^2\gamma}. \tag{24}$$

The function $\epsilon_{\mathrm{EP}}(x)$ is even in x and has a cusp at $x = 0$. EPs in the three-dimensional $\epsilon, \lambda, \gamma$ space form a 2D surface, represented in Fig. 2. Bifurcation diagrams of the

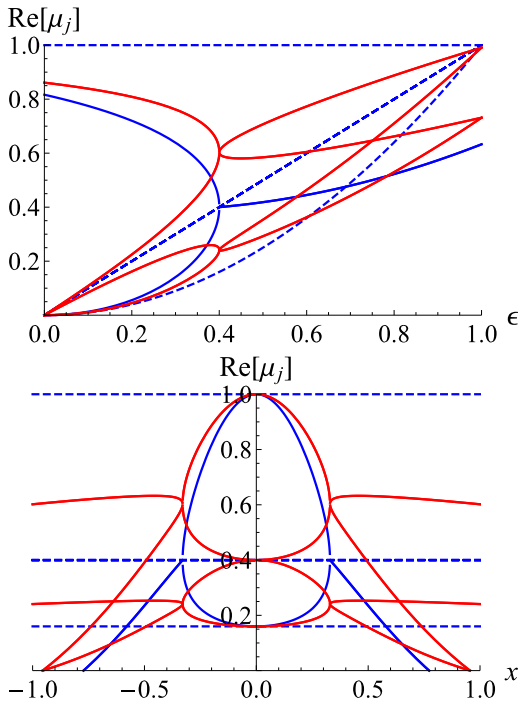


FIG. 3. Real part of $\mathcal{T}$ eigenvalues as a function of ϵ for fixed $\lambda = 1.39$ (top panel), and as a function of $\log\lambda$ for fixed $\epsilon = 0.4$ (bottom panel). In both cases $q = e^{i\pi/4}$. Red and blue curves correspond to $\mathcal{T}_+$ and $\mathcal{T}_-$, respectively, while dashed lines refer to analytic eigenvalues $\lambda_j = 1, \epsilon, \epsilon^2$. Bifurcation points occur at the EP (red dot), located on the EP manifold shown in Fig. 2.

superoperator eigenvalues as functions of ϵ and of $x = \log(\lambda)$ for parameter values corresponding to the point a and points b, c of Fig. 2, are depicted in Fig. 3 and in Fig. 6 of Appendix B, respectively.

V. SENSING PROPERTIES ON THE EP MANIFOLD

Liouvillian exceptional points are known to be associated with enhanced sensitivity to perturbations, originating from the nonanalytic dependence of the Liouvillian spectrum on external parameters. In particular, near a second-order LEP, small perturbations typically induce eigenvalue splittings scaling as $\sqrt{\varepsilon}$, leading to an amplified dynamical response compared to regular points in parameter space.

At an LEP, the discrete-time superoperator becomes nondiagonalizable. As a consequence of its Jordan-block structure, the stroboscopic evolution is no longer purely exponential but acquires polynomial prefactors, resulting in a contribution that grows linearly with the discrete time step n.

This anomalous time dependence is the discrete-time counterpart of the well-known non-Hermitian dynamical response at exceptional points and constitutes the fundamental mechanism underlying sensitivity enhancement in both continuous-time open quantum systems and non-Hermitian photonic platforms [1,3,4,6].

To illustrate the impact of EPs on dynamics we consider the discrete-time evolution of observables. For an initial state $\rho[0]$ the vectorized dynamics is

$$|\rho[n]\rangle = \mathcal{T}^n|\rho[0]\rangle, \tag{25}$$

with $\mathcal{T}$ the superoperator from Eq. (6). Away from EPs, $\mathcal{T}$ is diagonalizable and admits a biorthogonal set of left $\{\langle w_j|\}$ and right $\{|v_j\rangle\}$ eigenvectors, $\langle v_j|w_k\rangle = \delta_{jk}$. The expectation value of an observable $\hat{g}$ then reads

$$\langle\hat{g}[n]\rangle = \sum_{j=1}^{16}(\mu_j)^n\,\gamma_j, \quad \gamma_j = \alpha_j\,\mathrm{Tr}(\hat{g}\,\mathbf{v}_j), \tag{26}$$

where μ_j and $\mathbf{v}_j$ are the eigenvalues and eigenmatrices of $\mathcal{U}$, and $\alpha_j = \langle w_j|\rho[0]\rangle$ are expansion coefficients. Enhanced sensitivity arises when $\hat{g}$ has overlap with eigenvectors associated with an EP.

The cleanest effect of EP can be best seen on observables which have significant overlap with the EP-containing eigenvectors of the superoperator $\mathcal{T}$, and by choosing an appropriate initial state.

As a concrete example we consider an initially pure quantum state $\rho[0] = |\psi\rangle\langle\psi|$ with $\langle\psi| = 2^{-\frac{1}{2}}(1,0,1,0)$ and take the two-point operator

$$\hat{\mathbf{e}}_3 = \tfrac{1}{2}\sigma_1^-\big(I + \sigma_2^z\big), \tag{27}$$

whose dynamics involves only μ_9, μ_{10},

$$\langle\hat{\mathbf{e}}_3[n]\rangle = \sum_{j=9,10}(\mu_j)^n\gamma_j, \tag{28}$$

with coefficients

$$\gamma_9 = \frac{g_-}{2(4+g_-)}, \quad \gamma_{10} = \frac{g_+}{2(4+g_+)}, \tag{29}$$

and

$$g_\pm = \frac{[\lambda(q^2-1)(\epsilon-1)\pm Q]^2}{(\lambda^2-1)^2q^2\epsilon} \tag{30}$$

(for the explicit derivation of the above equations, see Appendix C). The time evolution of the quantity $|\langle\hat{\mathbf{e}}_3[n]\rangle|$ properly rescaled is shown in Fig. 4, at EP and its proximity. Everywhere except at the EP (black curve in the middle row), the numerical data perfectly match the analytic expression (28). An additional factor μ^{-n} in front of the $\langle\hat{\mathbf{e}}_3[n]\rangle$ is chosen so that to ensure that the quantity $|\mu^{-n}]\langle\hat{\mathbf{e}}_3[n]\rangle|$ enters a stable cycle for large n.

Three different regimes can be seen clearly. First, let us discuss the origin of the linear increase at EP (black curve, middle row at Fig. 4). At the EP two eigenvalues coincide $\mu_9 = \mu_{10} \equiv \mu_0$ and the respective 2×2 block B of the Liouvillian acquires a Jordan form

$$B = \begin{pmatrix}\mu_0 & 1\\ 0 & \mu_0\end{pmatrix}. \tag{31}$$

A repeated application of the above on a vector $\psi \in C_2$ gives

$$B^n\psi = \begin{pmatrix}\mu_0^n & n\mu_0^{n-1}\\ 0 & \mu_0^n\end{pmatrix}\psi. \tag{32}$$

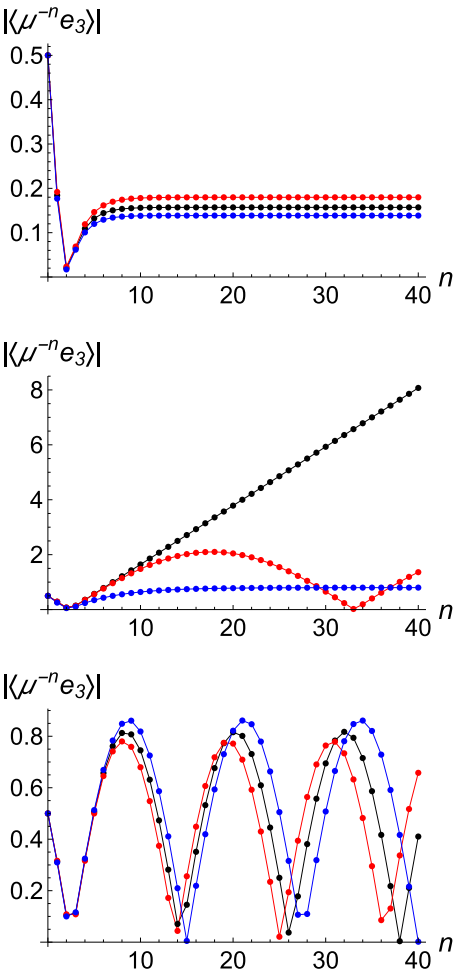


FIG. 4. Renormalized value of $|\langle\hat{\mathbf{e}}_3[n]\rangle|$ vs discrete time n, below EP $\epsilon \equiv \epsilon_0 = 0.32$, $0.32 \pm \delta$ (upper row), at EP $\epsilon = 0.4$, $0.4 \pm \delta$(middle row), and above EP $\epsilon = 0.48$, $0.48 \pm \delta$ with $\delta = 0.01$. Black, red, and blue curves correspond to $\epsilon = \epsilon_0$, $\epsilon_0 + \delta$, and $\epsilon_0 - \delta$, respectively. The Value of μ is chosen as $\mu = \max[|\mu_9(\epsilon)|, |\mu_{10}(\epsilon)|]$ at the respective ϵ. The Linear increase of $|\mu^{-n}\langle\hat{\mathbf{e}}_3[n]\rangle|$ at EP (black curve in the middle row) is due to nondiagonalizability of the Liouvillian at EP (see text). Other parameters: $q = \exp(i\pi/4)$, $\lambda = 1.390\,16$. The EP is located at $\epsilon_{\rm EP} = 0.4$ (point a in Fig. 2).

Assuming $\psi^T = (a, b)$ we obtain

$$\mu_0^{-n}||B^n\psi|| = \mu_0^{-n}\left|\left|\begin{pmatrix}\mu_0 & 1\\ 0 & \mu_0\end{pmatrix}^n\begin{pmatrix}a\\ b\end{pmatrix}\right|\right| = n|\mu_0^{-1}b|\left[1 + O\left(\frac{a}{bn}\right)\right], \tag{33}$$

e.g., an asymptotic linear increase with n, seen on the black curve, in the middle Panel of Fig. 4. Note that if at the point $\epsilon_{\rm EP} = 0.4$ the Liouvillian would have conventional degeneracy, i.e., $B = \mathrm{diag}(\mu_0, \mu_0)$, then it would result in a constant in time $\mu_0^{-n}||B^n\psi|| = ||\psi|| = \sqrt{|a|^2 + |b|^2}$.

At all the other points except EP we have a diagonalizable Liouvillian, with temporal evolution of the observable described by (28). Notably, however, there is an asymptotic constant behaviour of the absolute value of $\mu^{-n}\langle\hat{\mathbf{e}}_3[n]\rangle$ below EP $\epsilon < \epsilon_{\rm EP}$ and asymptotic periodic behavior above EP $\epsilon > \epsilon_{\rm EP}$. To explain this, let us take a look at the nature of the EP for μ_9, μ_{10} in Fig. 5: Above EP, absolute values of μ_9, μ_{10} are the same, while below EP, they are different. This straightforwardly explains the qualitative differences in Fig. 4 for $\epsilon < \epsilon_{\rm EP}$ and $\epsilon > \epsilon_{\rm EP}$.

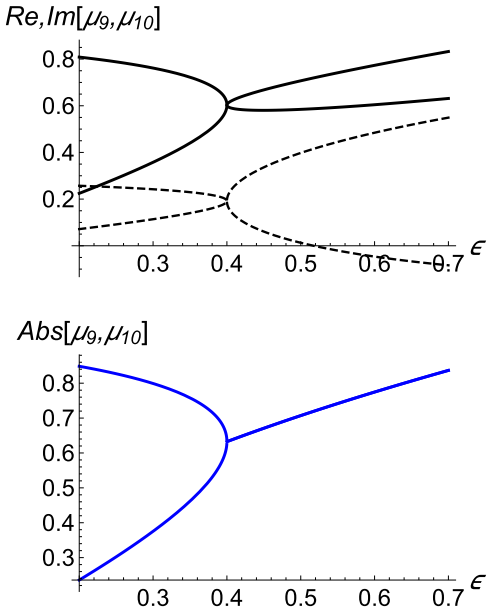


FIG. 5. μ_9, μ_{10}, entering Eq. (28) vs ϵ. EP is located at $\epsilon_{\rm EP} = 0.4$. The Bottom Panel shows absolute values $|\mu_9|$, $|\mu_{10}|$ while the Top panel shows their real part (solid lines) and the imaginary part (dashed lines). Other parameters are fixed as in Fig. 4.

VI. CONCLUSION

In this work, we have extended exceptional-point physics, traditionally formulated within continuous Lindbladian dynamics, to discrete architectures built from physical completely positive trace-preserving maps. In particular, we analytically demonstrated the existence of a full manifold of Liouvillian exceptional points in a minimal two-qubit brickwork CPTP circuit and showed that, in the vicinity of this manifold, the dynamics of observables exhibits the hallmark linear-in-time sensitivity enhancement. This establishes that discrete-time Liouvillian exceptional points preserve the essential dynamical features underlying the enhanced sensitivity known from their continuous-time counterparts.

From a practical perspective, operating a quantum circuit close to such an exceptional point implies that small perturbations of experimentally controllable parameters, such as gate angles or dissipative rates entering the CPTP maps, can induce parametrically enhanced changes in the evolution of the density matrix.

We note, however, that while the nonanalytic spectral response near the exceptional points leads to an amplified parameter dependence, a debate has emerged regarding whether this translates into a genuine metrological advantage in practical settings. Much of this discussion has focused on exceptional points in non-Hermitian Hamiltonians, often realized in postselected or classical wave systems, where the enhanced susceptibility can be accompanied by increased sensitivity to noise, potentially offsetting the gain [16,17]. In this

context, recent works have shown that non-Hermitian sensing schemes can outperform Hermitian ones under specific conditions, such as in the presence of technical noise, although such advantages do not necessarily rely solely on the presence of an exceptional point [18,19].

While our analysis focuses on establishing the existence and structure of Liouvillian EPs in stroboscopic quantum dynamics, it naturally motivates future investigations of concrete sensing protocols in open quantum circuits.

ACKNOWLEDGMENTS

V.P. acknowledges support by ERC Advanced Grant No. 101096208–QUEST, Research Program Grant No. P1-0402, and Grant No. N1-0368 of Slovenian Research and Innovation Agency (ARIS) and by Deutsche Forschungsgemeinschaft through DFG Project No. KL645/20-2. V.P. wishes to thank the Department of Physics of the University of Salerno, where this project initiated, both for hospitality and partial financial support.

DATA AVAILABILITY

The data that support the findings of this article are not publicly available. The data are available from the authors upon reasonable request.

APPENDIX A: KRAUS MAP AND CONTINUOUS-TIME LIMIT OF THE QUBIT CIRCUIT DYNAMICS

The dissipative channel acting on one of the qubits is defined as $\mathcal{K}[\cdot] = \sum_{j=1}^{2} K_j[\cdot]K_j^\dagger$ with Kraus operators

$$K_1(\epsilon) = \sqrt{1-\epsilon^2}\,\sigma_1^+, \quad K_2(\epsilon) = \begin{pmatrix} 1 & 0 \\ 0 & \epsilon \end{pmatrix}. \tag{A1}$$

This channel is completely positive and trace preserving by construction, as $\sum_j K_j^\dagger K_j = \mathbb{I}$. The eigenoperators of $\mathcal{K}$ are $\psi_0 = |\uparrow\rangle\langle\uparrow|$, $\psi_1 = \sigma^z$, $\psi_2 = \sigma^+$, $\psi_3 = \sigma^-$, with corresponding eigenvalues $\lambda_0 = 1, \lambda_1 = \epsilon^2$, $\lambda_2 = \lambda_3 = \epsilon$. These coincide with those of the channel generated by the Lindblad dissipator $\exp(\Gamma t\, \mathcal{D}_{\sigma^+})$,

$$\mathcal{D}_L[\rho] = 2L\rho L^\dagger - \{L^\dagger L, \rho\}, \tag{A2}$$

whose spectrum is $\mu_0 = 1$, $\mu_1 = e^{-2\Gamma t}$, $\mu_2 = \mu_3 = e^{-\Gamma t}$. The equivalence $\mathcal{K}^n \simeq \exp(\Gamma t\, \mathcal{D}_{\sigma^+})$ follows in the scaling limit $\epsilon = e^{-\Gamma t/n}$, $n \to \infty$. The complete update of the density matrix over one step reads

$$\rho_{t+1} = U\left(\sum_{j=1}^{2}(K_j \otimes V)\rho_t(K_j^\dagger \otimes V^\dagger)\right)U^\dagger = \mathcal{U}\,\rho_t, \tag{A3}$$

where U is the two-qubit fSim gate defined in Eq. (1) of the main text and V is an arbitrary 2×2 unitary matrix.

In the weak-coupling limit $\lambda = 1 + \epsilon$ with $\epsilon = (q - q^{-1})t/(in)$ and n very large, we obtain $U \approx I - i\frac{t}{n}h$, where $h = \sigma^x \otimes \sigma^x + \sigma^x \otimes \sigma^x + \frac{q+q^{-1}}{2}(\sigma^z \otimes \sigma^z - I)$ is the density of the XXZ spin chain Hamiltonian. Then, using the Trotter formula, one obtains $\lim_{n\to\infty} \mathcal{U}^n\rho = e^{\mathcal{L}t}\rho$ where $\mathcal{L}$ is the Liouvillian dynamics of the boundary-driven Lindblad master equation

$$\frac{\partial\rho}{\partial t} = \mathcal{L}[\rho] = -i[H, \rho] + \Gamma\mathcal{D}_{L_{\sigma_1^+}}[\rho], \tag{A4}$$

where $H = \sum_{n=1}^{N-1} h_{n,n+1}$ is the XXZ spin chain Hamiltonian. Thus, the brickwork circuit can be seen as a generalization of a Trotter discretization of Lindblad dynamics.

APPENDIX B: EXPLICIT FORM OF THE LIOUVILLIAN BLOCKS

In a convenient basis obtained by a similarity transformation within each parity sector, the 4×4 blocks $A_\pm$, $B_\pm$, $C_\pm$, $D_\pm$ in Eq. (10) are

$$A_+ = \begin{pmatrix} 1 & 0 & 0 & 0 \\ 0 & \epsilon^2 & 0 & 0 \\ 0 & 0 & \epsilon & 0 \\ 0 & 0 & 0 & \epsilon \end{pmatrix}, \quad B_+ = \begin{pmatrix} 0 & 1-\epsilon^2 & 0 & 0 \\ 0 & 0 & 0 & 0 \\ 0 & 0 & 0 & 0 \\ 0 & 0 & 0 & 0 \end{pmatrix},$$

$$C_+ = \begin{pmatrix} 0 & 0 & a_1(1-\epsilon^2) & 0 \\ 0 & 0 & a_3(1-\epsilon^2) & 0 \\ 0 & 0 & -a_2(1-\epsilon^2) & 0 \\ 0 & 0 & a_2(1-\epsilon^2) & 0 \end{pmatrix}, \quad D_+ = \begin{pmatrix} a_1 & a_3\epsilon^2 & -a_2\epsilon & a_2\epsilon \\ a_3 & a_1\epsilon^2 & a_2\epsilon & -a_2\epsilon \\ -a_2 & a_2\epsilon^2 & a_1\epsilon & a_3\epsilon \\ a_2 & -a_2\epsilon^2 & a_3\epsilon & a_1\epsilon \end{pmatrix},$$

$$A_- = \begin{pmatrix} b_3 & 0 & b_4\epsilon & 0 \\ 0 & b_3\epsilon^2 & 0 & b_4\epsilon \\ b_4 & 0 & b_3\epsilon & 0 \\ 0 & b_4\epsilon^2 & 0 & b_3\epsilon \end{pmatrix}, \quad B_- = \begin{pmatrix} 0 & b_3(1-\epsilon^2) & 0 & 0 \\ 0 & 0 & 0 & 0 \\ 0 & b_4(1-\epsilon^2) & 0 & 0 \\ 0 & 0 & 0 & 0 \end{pmatrix},$$

$$C_- = \begin{pmatrix} 0 & b_1(1-\epsilon^2) & 0 & 0 \\ 0 & 0 & 0 & 0 \\ 0 & 0 & 0 & 0 \\ 0 & b_1(\epsilon^2-1) & 0 & 0 \end{pmatrix}, \quad D_- = \begin{pmatrix} b_1 & 0 & 0 & -b_2\epsilon \\ 0 & b_1\epsilon^2 & -b_2\epsilon & 0 \\ 0 & -b_2\epsilon^2 & b_1\epsilon & 0 \\ -b_2 & 0 & 0 & b_1\epsilon \end{pmatrix},$$

with coefficients a_i, b_i given by

$$a_1 = \frac{\lambda^2(q^2-1)^2}{(q^2-\lambda^2)(\lambda^2q^2-1)}, \quad a_2 = \frac{\lambda(\lambda^2-1)q(q^2-1)}{(q^2-\lambda^2)(\lambda^2q^2-1)}, \quad a_3 = -\frac{(\lambda^2-1)^2q^2}{(q^2-\lambda^2)(\lambda^2q^2-1)}, \tag{B1}$$

$$b_1 = \frac{\lambda(q^2-1)}{q^2-\lambda^2}, \quad b_2 = \frac{(\lambda^2-1)q}{q^2-\lambda^2}, \quad b_3 = \frac{\lambda(q^2-1)}{\lambda^2q^2-1}, \quad b_4 = \frac{(\lambda^2-1)q}{\lambda^2q^2-1}. \tag{B2}$$

Note that most of the above blocks are sparse, a property that enables an analytic evaluation of the eigenvalues of $\tau_\pm$ using the Schur-complement formula in Eq. (11). In Fig. 6 we show various types of bifurcation diagrams for the eigenvalues of the Liouvillian as obtained from the above block decomposition using Eq. (11).

APPENDIX C: TIME EVOLUTION OF THE OBSERVABLES: DERIVATION OF EQS. (28)–(30)

The diagonalizability of the superoperator $\mathcal{T}$ in Eq. (4) implies the existence of the biorthogonal set of its left and right eigenvectors $\langle w_j|$, $|u_j\rangle$, corresponding to the eigenvalues μ_j of $\mathcal{T}$ and satisfying $\langle w_j|u_k\rangle = \delta_{j,k}$.

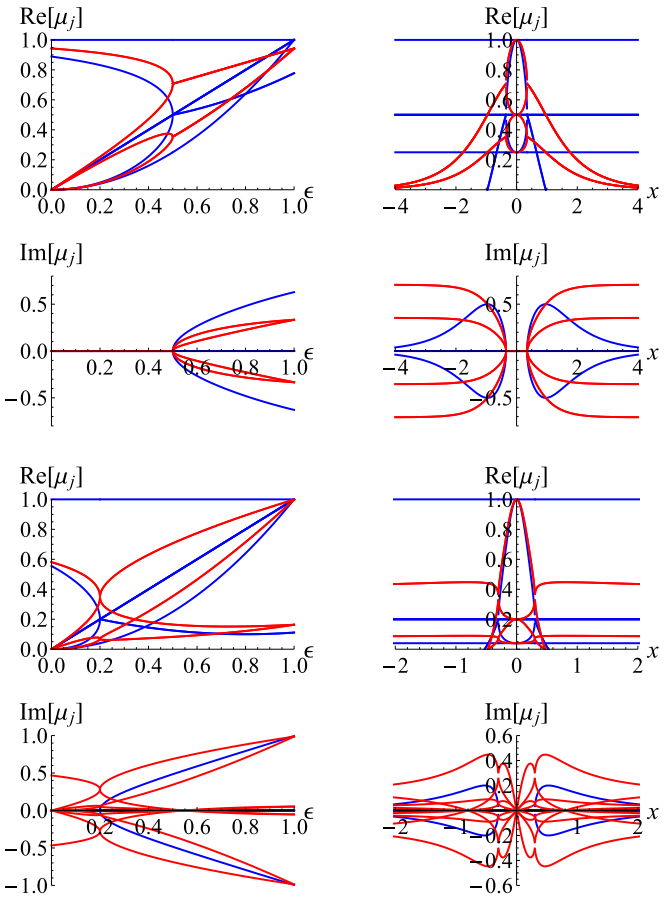


FIG. 6. Real and imaginary parts of the superoperator eigenvalues corresponding to blocks τ_+ (blue color) and τ_- (red color) in (9), vs ϵ (left column) and $x = \log(\lambda)$ (right column), for parameter values corresponding to points b (first and second row panels) and c (third and fourth row panels) in Fig. 2 in the main text.

The time evolution of an observable $\hat{g}$ is given by

$$\langle \hat{g}[n]\rangle = \mathrm{tr}\,(\hat{g}\,\rho[n]), \tag{C1}$$

where $\rho[n] = \mathcal{U}^n\rho[0]$ is a reduced density matrix of the system after n steps. Using biorthogonal basis of the vectorized version $\mathcal{T}$ of the map $\mathcal{U}$ we write

$$|\rho[n]\rangle = \sum_{j=1}^{16}(\mu_j)^n\langle w_j|\rho[0]\rangle|v_j\rangle, \tag{C2}$$

where $|\rho[n]\rangle$ is a vectorized density matrix after n steps. Using $\langle g|$ for the vectorized version of $\hat{g}$ we obtain

$$\langle \hat{g}[n]\rangle = \sum_{j=1}^{16}(\mu_j)^n\langle w_j|\rho[0]\rangle\langle g|v_j\rangle. \tag{C3}$$

In order to see clearly the effect of EP, we need to choose $\rho[0]$ and $\hat{g}$ such that the major contribution in (C3) comes from some of EP-containing eigenvalues $\mu_7, \mu_8, \ldots, \mu_{16}$.

First, we list all the $|v_j\rangle$. using standard notation $(e_j)_k = \delta_{jk}$, we have the following: for the regular analytic $\mathcal{T}$ eigenvalues $\mu_1, \mu_2, \ldots, \mu_6$ the eigenvectors are

$$|v_1\rangle = e_1, \tag{C4}$$

$$|v_2\rangle = e_1 - e_6 - e_{11} + e_{16}, \tag{C5}$$

$$|v_{3,4}\rangle = (1+\epsilon)e_1 + x_4e_4 - \epsilon e_6 + Fe_{10} - e_{11} + x_{13}e_{13}, \tag{C6}$$

$$|v_{5,6}\rangle = (1+\epsilon)e_1 + x_4e_4 - \epsilon e_6 - Fe_7 - e_{11} + x_{13}e_{13}, \tag{C7}$$

$$F = \frac{(1-q^2)(\epsilon-1)\lambda}{q(-1+\lambda^2)}, \tag{C8}$$

where x_4, x_{13} are arbitrary constants. The EP-containing eigenvalues contain dependence on the square root Q from (21), namely,

$$|v_7\rangle = a_1e_1 + \sum_{j=6,7,10,11} b_j(Q)e_j, \tag{C9}$$

a_j are analytic coefficients while $b_j(Q)$ are linear in Q. Then,

$$|v_8\rangle = -|v_7\rangle + 2Q[-\lambda(q^2-1)](e_6 - e_{11}) + 2Q(\lambda^2-1)q(e_7 - e_{10}). \tag{C10}$$

$|v_9\rangle$, $|v_{10}\rangle$ have the especially simple form

$$|v_9\rangle = e_5 - \frac{Q - \lambda(q^2-1)(\epsilon-1)}{2(\lambda^2-1)q\epsilon}e_9, \tag{C11}$$

$$|v_{10}\rangle - |v_9\rangle = -\frac{Q}{(\lambda^2-1)q\epsilon}e_9. \tag{C12}$$

Now, $|v_{11,12,\ldots,16}\rangle$ are given by

$$|v_{11}\rangle, |v_{12}\rangle = e_{12} + \sum_{j=2,3,8} d_j(Q)e_j, \tag{C13}$$

$$|v_{13}\rangle = e_2 + \frac{Q - \lambda(q^2-1)(\epsilon-1)}{2(\lambda^2-1)q\epsilon}e_3, \tag{C14}$$

$$|v_{14}\rangle - |v_{13}\rangle = \frac{Q}{q\epsilon(1-\lambda^2)}e_3, \tag{C15}$$

$$|v_{15}\rangle, |v_{16}\rangle = e_{15} + \sum_{j=5,9,14} f_j(Q)e_j, \tag{C16}$$

where f_j are some rational expressions containing Q whose explicit form will not be needed in the following. The explicit form of the left eigenvectors $\langle w_j|$ can be written as well. With explicit sets $|v_j\rangle$ and $\langle w_j|$ we are in principle able to calculate fully analytically, a time evolution for an arbitrary initial state $\rho[0]$.

Below we shall just give information regarding the chosen observable.

To proceed let us denote by $\hat{\mathbf{e}}_j$ an operator, the vectorized version of which is $|\hat{\mathbf{e}}_j\rangle = e_j$. From (C12) and (C15), we find that among the simplest observables $\mathbf{e}_j$, the two observables

$$\hat{\mathbf{e}}_3 = \tfrac{1}{2}\sigma_1^-\big(I + \sigma_2^z\big), \quad \hat{\mathbf{e}}_9 = \tfrac{1}{2}\sigma_1^+\big(I + \sigma_2^z\big) = \mathbf{e}_3^\dagger, \tag{C17}$$

are most sensitive to the presence of EP, since they have an overlap with only EP-containing eigenvectors. Indeed, from easily verifiable $\mathrm{Tr}(\mathbf{e}_3\mathbf{e}_j) = \delta_{j,9}$, $\mathrm{Tr}(\mathbf{e}_9\mathbf{e}_j) = \delta_{j,3}$, and inspecting (C4)–(C16), we find that $\mathbf{e}_9$ has a nontrivial overlap with $|v_{11}\rangle, |v_{12}\rangle, |v_{13}\rangle, |v_{14}\rangle$ only, all of which are EP-containing eigenvectors. Likewise, $\mathbf{e}_3$ has a nontrivial overlap only with $|v_9\rangle, |v_{10}\rangle, |v_{15}\rangle, |v_{16}\rangle$.

Let us choose an observable $\mathbf{e}_3$ for definiteness. From (C3), we have

$$\langle \hat{e}_3[n]\rangle = \sum_{j=9,10,15,16} (\mu_j)^n \langle w_j|\rho[0]\rangle\langle \hat{e}_3|v_j\rangle \tag{C18}$$

(note that $\langle \hat{e}_3|e_j\rangle = \delta_{j,9}$). To calculate the above, we need the explicit form of $\langle w_j|$ for $j = 9, 10, 15, 16$. We find

$$\langle w_{15}| = \frac{q(\lambda^2-1)}{Q}(e_{14} - f_- e_{15}), \tag{C19}$$

$$\langle w_{16}| = -\frac{q(\lambda^2-1)}{Q}(e_{14} - f_+ e_{15}), \tag{C20}$$

$$\left(1 + \frac{f_-^2}{\epsilon}\right)\langle w_9| = e_5 + f_-\, e_9 + X_{14}e_{14} + X_{15}e_{15}, \tag{C21}$$

$$\left(1 + \frac{f_+^2}{\epsilon}\right)\langle w_{10}| = e_5 + f_+\, e_9 + Y_{14}e_{14} + Y_{15}e_{15}, \tag{C22}$$

$$f_\pm = \frac{\lambda(q^2-1)(\epsilon-1) \pm Q}{2(\lambda^2-1)q}, \tag{C23}$$

where $X_{14}, X_{15}, Y_{14}, Y_{15}$ are coefficients given by some complicated ratios, the explicit form of which will not be needed in the following. To simplify the calculus further, we choose $\rho[0]$ to be a pure state of the form

$$\rho[0] = |\psi\rangle\langle\psi|, \quad \langle\psi| = \frac{1}{\sqrt{2}}\langle 1, 0, 1, 0|, \tag{C24}$$

which has no overlaps with w_{15}, w_{16}: $(w_{15}, |\rho[0]\rangle) = (w_{16}, |\rho[0]\rangle) = 0$. Then the summation in (C18) extends over $j = 9, 10$ only. Denoting $\langle w_j|\rho[0]\rangle\langle \hat{e}_3|v_j\rangle \equiv \gamma_j$, we find

$$\langle \hat{e}_3[n]\rangle = \sum_{j=9,10,15,16} (\mu_j)^n \gamma_j, \tag{C25}$$

$$\gamma_{15} = \gamma_{16} = 0, \tag{C26}$$

$$\{\gamma_9, \gamma_{10}\} = \left\{\frac{g_-}{2(4+g_-)}, \frac{g_+}{2(4+g_+)}\right\}, \tag{C27}$$

$$g_\pm = \frac{(\lambda(q^2-1)(\epsilon-1) \pm Q)^2}{(\lambda^2-1)^2q^2\epsilon} = 4\epsilon^{-1}(f_\pm)^2, \tag{C28}$$

i.e., Eqs. (28)–(30) of the main text.

[1] F. Minganti, A. Miranowicz, R. W. Chhajlany, and F. Nori, Quantum exceptional points of non-Hermitian Hamiltonians and Liouvillians: The effects of quantum jumps, Phys. Rev. A **100**, 062131 (2019).

[2] I. I. Arkhipov, A. Miranowicz, F. Minganti, and F. Nori, Quantum and semiclassical exceptional points of a linear system of coupled cavities with losses and gain within the Scully-Lamb laser theory, Phys. Rev. A **101**, 013812 (2020).

[3] W. Chen, S. K. Özdemir, G. Zhao, J. Wiersig, and L. Yang, Exceptional points enhance sensing in an optical microcavity, Nature (London) **548**, 192 (2017).

[4] H. Hodaei, A. U. Hassan, S. Wittek, H. Garcia-Gracia, R. El-Ganainy, D. N. Christodoulides, and M. Khajavikhan, Enhanced sensitivity at higher-order exceptional points, Nature (London) **548**, 187 (2017).

[5] Y.-H. Lai, Y.-K. Lu, M.-G. Suh, Z. Yuan, and K. Vahala, Observation of the exceptional-point-enhanced Sagnac effect, Nature (London) **576**, 65 (2019).

[6] S. Özdemir, S. Rotter, F. Nori, and L. Yang, Parity–time symmetry and exceptional points in photonics, Nat. Mater. **18**, 783 (2019).

[7] R. Huang, S. K. Özdemir, J.-Q. Liao, F. Minganti, L.-M. Kuang, F. Nori, and H. Jing, Exceptional photon blockade: engineering photon blockade with chiral exceptional points, Laser Photonics Rev. **16**, 2100430 (2022).

[8] W. Chen, M. Abbasi, B. Ha, S. Erdamar, Y. N. Joglekar, and K. W. Murch, Decoherence-induced exceptional points in a dissipative superconducting qubit, Phys. Rev. Lett. **128**, 110402 (2022).

[9] V. Popkov, C. Presilla, and M. Salerno, Manifolds of exceptional points and effective Zeno limit of an open two-qubits system, Phys. Rev. A **111**, L050202 (2025).

[10] X.-D. Hu and D.-B. Zhang, Exact correlation functions for dual-unitary quantum circuits with exceptional points, Phys. Rev. B **111**, 024301 (2025).

[11] M. Vanicat, L. Zadnik, and T. Prosen, Integrable trotterization: local conservation laws and boundary driving, Phys. Rev. Lett. **121**, 030606 (2018).

[12] M. Ljubotina, L. Zadnik, and T. Prosen, Ballistic spin transport in a periodically driven integrable quantum system, Phys. Rev. Lett. **122**, 150605 (2019).

[13] B. Bertini, P. Kos, and T. Prosen, Exact correlation functions for dual-unitary lattice models in 1+1 dimensions, Phys. Rev. Lett. **123**, 210601 (2019).

[14] X. Mi, A. A. Michailidis, S. Shabani, K. C. Miao, P. V. Klimov, J. Lloyd, E. Rosenberg, R. Acharya, I. Aleiner, T. I. Andersen, *et al.*, Stable quantum-correlated many-body states through engineered dissipation, Science **383**, 1332 (2024).

[15] A. Morvan, T. I. Andersen, X. Mi, C. Neill, A. Pethucov, K. Kechedzhik, D. A. Abanin, A. Michailidis, R. Acharya, F. Arute, *et al.*, Formation of robust bound states of interacting microwave photons, Nature (London) **612**, 240 (2022).

[16] W. Ding, X. Wang, and S. Chen, Fundamental sensitivity limits for non-hermitian quantum sensors, Phys. Rev. Lett. **131**, 160801 (2023).

[17] N. Zeng, T. Liu, K. Xia, Y.-R. Zhang, and F. Nori, Non-Hermitian sensing from the perspective of postselected measurements, Phys. Rev. Res. **7**, 043219 (2025).

[18] I. I. Arkhipov, F. Nori, and S. K. Özdemir, Achieving the quantum Fisher information bound in pseudo-Hermitian sensors, Phys. Rev. Lett. **136**, 080802 (2026).

[19] K. Yang, Y. Chu, N. Wang, and J. Cai, Practical advantage of non-Hermitian enhanced quantum sensing, arXiv:2603.20612.